Sensors and Materials, Vol. 37, No. 6 (2025) 2199–2221
MYU Tokyo

S & M 4051

Theoretical Model for Analyzing Cross-axis Sensitivity in 2D MEMS Accelerometer

Nguyen Van Cuong,[1] Nguyen Van Duong,[2] Bui Van Cuong,[1] and Chu Manh Hoang[3*]

[1]Faculty of Mechanical Engineering, Le Quy Don Technical University
No. 236 Hoang Quoc Viet Street, Bac Tu Liem, Hanoi 100000, Vietnam
[2]FPT University Hoa Lac High Tech Park, Hanoi 100000, Vietnam
[3]School of Materials Science and Engineering, Hanoi University of Science and Technology
No. 1 Dai Co Viet Street, Hai Ba Trung, Hanoi 100000, Vietnam

(Received March 10, 2025; accepted May 14, 2025)

Keywords: Two-axis MEMS accelerometer, air damping, fabrication error, cross-axis sensitivity

Micro-electromechanical system (MEMS)-based sensors play a vital role in the future of smart sensing applications owing to their small size, low power consumption, and cost-effectiveness. The issue of cross-axis sensitivity is of utmost importance when designing two-dimensional acceleration sensors. In this paper, we present the design of a two-dimensional acceleration sensor and investigate how the vibrations in different directions affect its sensitivity. A theoretical model, in which the effects of fabrication errors and air damping are considered, is built to investigate the sensor's operation characteristics and optimize the sizes of the sensor's spring systems in order to reduce cross-axis sensitivity. The results show that the cross-axis sensitivities in two-dimensional acceleration sensors have very small values, namely, 0.014% in the *X*-direction and 0.00649% in the *Y*-direction. The findings of this study are useful for the computation and development of two-dimensional acceleration sensors for high-precision measurements.

1. Introduction

The development of micro-electromechanical system (MEMS) technology has resulted in the production of a wide range of small-scale devices, namely, accelerometers.(1) Acceleration sensors can be one-, two-, or three-axis accelerometers.(2) Acceleration sensors are extensively used in many areas, including portable mobile devices and the aerospace industry.(3–5) They are employed in motion sensing for wearable devices and smartphones to detect changes in orientation and gestures. They are also employed in tilt sensing for level sensors and inclinometers to measure tilt angles. Furthermore, two-axis accelerometers are utilized in industrial equipment to measure vibrations along two axes. Stabilization systems are included in camera stabilization systems and drones to counteract motions along two axes. Accelerometers exhibit various parameters based on their unique use, such as sensitivity, bandwidth, offset, nonlinearity, and cross-axis sensitivity. Of these factors, cross-axis sensitivity is particularly

*Corresponding author: e-mail: hoangcm@itims.edu.vn, hoang.chumanh@hust.edu.vn
https://doi.org/10.18494/SAM5617

ISSN 0914-4935 © MYU K.K.
https://myukk.org/

important for high-precision measurements.[6,7] The cross-axis sensitivity corresponds to the measured output signal along a sensor axis while acceleration is applied along its orthogonal axis. The cross-axis error is usually caused by faults in fabrication or design problems. The cross-axis sensitivity is often quantified as a percentage, which is determined by dividing the sensitivity measured in the cross-direction by that recorded in the sensing direction. A few models of one-axis accelerometers with low cross-axis sensitivity have been reported. They are based on an improved suspended spring system, which is compliant with the sensing direction while being robust to other undesired vibration directions.[8–11] For example, Qifang *et al.* developed a highly symmetric MEMS sandwich accelerometer using a double-device-layer silicon-on-insulator wafer.[9] In their design, a proof mass is suspended by two layers of L-shaped beams symmetrically arranged on the upper and lower device layers. With such a two-layer spring system design, the single-axis (z-axis) sensing mode of the accelerometer is successfully decoupled from other variation modes. The cross-axis sensitivity of the accelerometer is as low as 0.356%. Jianqiang *et al.* designed a piezoresistive accelerometer consisting of a proof mass, eight supporting beams, and four sensing beams.[11] The gravity center of the proof mass lies within the neutral plane of the supporting beams. Experimental results show that the cross-axis sensitivities under X and Y accelerations are only 1.67 and 0.82%, respectively, compared with the z-axis sensitivity. Two-axis acceleration sensor models have also been introduced in the literature.[12,13] In these models, a proof mass is directly suspended by straight beam springs that are simultaneously compliant to two orthogonal sensing directions. For these models, displacement in one direction is related to the remaining direction. Therefore, this causes the cross-axis sensitivity to increase. Several two-axis displacement models capable of decoupling the two orthogonal sensing directions have been introduced. In these models, the proof mass is connected to a frame by a straight beam system.[14] The frame is suspended by another straight beam system that is orthogonal to the proof mass's suspension spring system. Thus, the proof mass and the frame are independently compliant to the two orthogonal displacement directions. Multiple-axis MEMS gyroscope/accelerometers with such decoupled structures have been proposed.[15] In addition, it is well known that the folded beam springs have advantages in designing the stable, large-displacement actuators.[16] However, there are no reports on the two-axis accelerometer with decoupled x- and y-sensing directions using folded beam springs. Furthermore, the sensors can use sensing mechanisms such as capacitive, piezoresistive, optical, and magnetic sensing mechanisms.[17] Micromachined accelerometers with a capacitive sensing mechanism have the advantages of high sensitivity, low noise, low temperature sensitivity, and low power consumption.[18] A differential capacitive sensing mechanism has also been explored and found to exhibit high linearity and large signal-to-noise ratio.[19] On the other hand, the dynamic behavior of most MEMS accelerometers is greatly affected by the movement of microstructures in an air environment.[20] MEMS accelerometers exhibit two main forms of damping: squeeze-film air damping and slide-film air damping. Squeeze-film air damping is accomplished through the interactions between the sensing and comb electrodes, while slide-film air damping is achieved through the movement of the proof mass in response to input acceleration.[21,22] Although there are reports on design models and experimental works on two-axis acceleration sensors, a theoretical model for investigating the operation characteristics of two-axis acceleration sensors, including their oscillation amplitudes and sensitivities, and the effect of manufacturing errors on cross-axis sensitivities, has not yet been reported.

In this work, we present a design of a two-axis MEMS accelerometer that utilizes the capacitive sensing mechanism. The sensor has low cross-axis sensitivity as a result of employing suspension springs that are compliant to the desired movement while being robust to other undesired movements. A comprehensive analytical model for investigating the operation characteristics and the cross-axis sensitivity of the two-axis MEMS accelerometer is built on the basis of elastic mechanical theory and air flow dynamics.

2. Model of Two-axis MEMS Accelerometer

The design of the sensor is shown in Figs. 1(a)–1(c). It consists of an outer movable frame M_1 linked to the fixed frames by four folded springs (K_1) and a proof mass M_2 connected to frame M_1 by four U-shaped springs (K_2). Here, we have used the folded beam springs, which have been commonly used in designing the decoupling systems. The model in Fig. 1 provides an overview of the sensor's structural components, and the actual scale has been omitted. Additionally, there are sets of two comb electrodes, arranged as shown in Fig. 1(a), to detect the sensor's acceleration in both the *X*- and *Y*-directions. The differential, parallel-plate capacitor sensing mechanism is used for detecting accelerations. In this mechanism, capacitance variation is based on the perpendicular displacement of the movable comb electrodes to the fixed comb electrodes. If the sensor is operated in the *X*-direction, the outer comb electrodes will act as a differential capacitive sensor to detect acceleration in the *X*-direction, while the inner comb electrodes will move parallel to each other without limiting the movement. For sensing acceleration in the *Y*-direction, the explanation is the same as that in the *X*-direction. Therefore, the overlap length

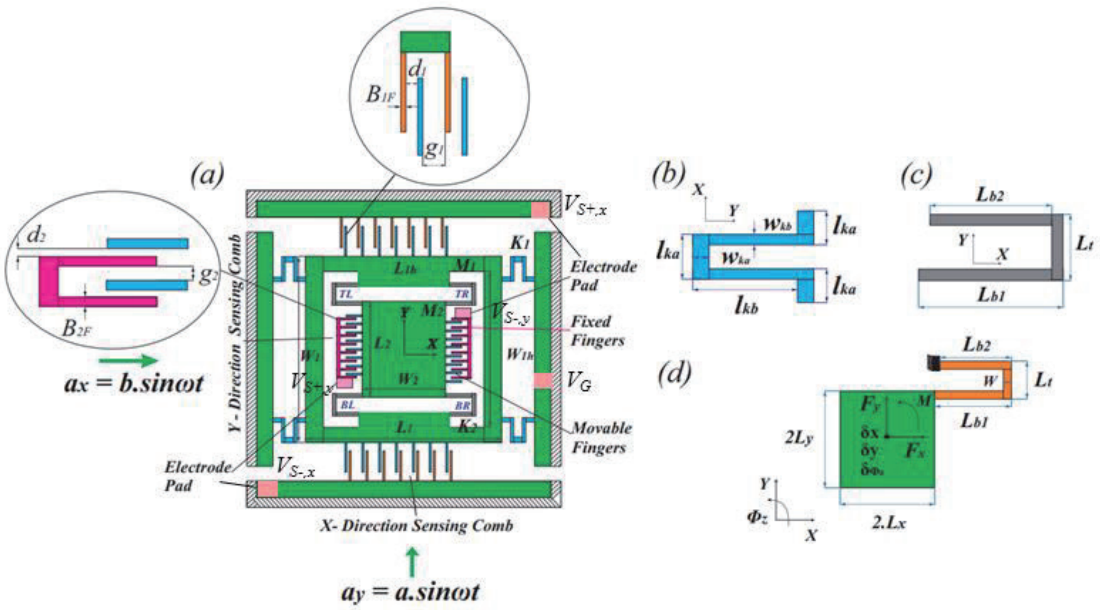

Fig. 1. (Color online) (a) Sensor model with the outer movable frame M_1 and inner mass M_2. (b) Dimensions of a single-fold spring (K_1). (c) Dimensions of a U-shaped spring with different beam length (K_2). (d) Forces and moments applied at the centroid of a proof mass attached to the free end of a U-shaped spring.

of the comb electrodes does not affect the sensor's movement in the *X*- and *Y*-directions. However, the asymmetrical design of comb electrodes can cause the electrostatic rotation moment. To eliminate this effect, we can use a symmetrical design of comb electrodes and/or a robust mechanical design that is only compliant with oscillations in the *X*- and *Y*-directions. Furthermore, for a non-ideal decoupling design, the movement of sensing comb electrodes in one direction will affect the movement in the remaining direction. The dimensional parameters of the sensor are denoted in Figs. 1(a) –1(c). The values of these parameters are shown in Table 1 for the outer movable frame M_1, the inner proof mass M_2, and sensing comb fingers, and in Table 2 for the springs K_1 and K_1.

Here, we consider two orthogonal oscillation systems, one along the *X*-axis and the other along the *Y*-axis. The spring constants of the first system with four folded springs in the directions of the *X*- and *Y*-axes, K_{1x} and K_{1y}, are respectively evaluated using[23]

$$K_{1x} = \frac{48EI_{z,b}\left[3\tilde{l}_{ka} + 2l_{kb}\right]}{2l_{kb}^2\left(12\tilde{l}_{ka}^2 + 12\tilde{l}_{ka}l_{kb} + 2l_{kb}^2\right)}, \tag{1}$$

Table 1
Parameters of the outer movable frame M_1, the inner proof mass M_2, and sensing comb fingers.

Component	Parameters (symbol)	Values
Outer movable frame M_1	Length (L_1); width (W_1); height (H_1)	4000 µm; 4000 µm; 20 µm
	Length (L_{1h}); width (W_{1h}); height (H_{1h})	2000 µm; 2000 µm; 20 µm
Proof mass M_2	Length (L_2); width (W_2); height (H_2)	1900 µm; 1600 µm; 20 µm
Sensing comb fingers	Overlapping length (Lv_1); width of movable comb (B_1); width of fixed comb (B_{1F}); thickness (T_{k1}); gap distance (d_1); lager gap distance (g_1); number of movable comb fingers (N_1)	100 µm; 5 µm; 5 µm; 20 µm; 1.5 µm; 3 µm; 400
Inner sensing comb fingers	Overlapping length (L_{v2}); width of movable comb (B_2); width of fixed comb (B_{2F}); thickness (T_{k2}); gap distance (d_2); lager gap distance (g_2); Number of movable comb fingers (N_2)	100 µm; 5 µm; 5 µm; 20 µm; 1.5 µm; 3 µm; 200

Table 2
Parameters of springs K_1 and K_2.

Component	Parameters (symbol)	Values
K_1	Thickness of folded spring (h)	20 µm
	Length of one beam (l_{kb})	160 µm
	Width of one beam (w_{kb})	15 µm
	Width of connection beam (w_{ka})	35 µm
	Length of connection beam (l_{ka})	35 µm
	Spring constant of folded springs in *X*-direction (K_{1x})	5167 N/m
	Spring constant of folded springs in *Y*-direction (K_{1y})	35989 N/m
K_2	Thickness of U-shaped spring (h)	20 µm
	Length of connecting beam between M_2 and M_1 (L_{b2})	160 µm
	Width of connecting beam between M_2 and M_1 (L_{b1})	170 µm
	Width of U-shaped spring beam (w)	10 µm
	Length of connecting beam (L_t)	25 µm
	Spring constant of U-shaped springs in *X*-direction (K_{2x})	123805 N/m
	Spring constant of U-shaped springs in *Y*-direction (K_{2y})	1417 N/m

$$K_{1y} = \frac{48EI_{z,b}}{3l_{ka}^2\left[9\tilde{l}_{ka} + 2l_{kb}\right]}. \tag{2}$$

Here, $I_{z,a} = hw_{ka}^3/12$ is the inertial moment of the beam with length l_{ka}, $I_{z,b} = hw_{kb}^3/12$ is the inertial moment of the beam with length l_{kb}, and $\tilde{l}_{ka} = I_{z,b}l_{ka}/I_{z,a}$. The Young's modulus of silicon, E, is 168.9 GPa.

The ratio between the spring stiffness K_1 in the X-axis direction and that in the Y-axis direction is derived as

$$\frac{K_{1y}}{K_{1x}} = \frac{2}{3}\left(\frac{l_{kb}}{l_{ka}}\right)^2 \frac{12\left(\frac{w_{kb}}{w_{ka}}\right)^6 + 12\left(\frac{w_{kb}}{w_{ka}}\right)^3 \frac{l_{kb}}{l_{ka}} + 2\left(\frac{l_{kb}}{l_{ka}}\right)^2}{27\left(\frac{w_{kb}}{w_{ka}}\right)^6 + 24\left(\frac{w_{kb}}{w_{ka}}\right)^3 \frac{l_{kb}}{l_{ka}} + 4\left(\frac{l_{kb}}{l_{ka}}\right)^2}. \tag{3}$$

The spring constants of the second system with four U-shaped springs in the directions of the X- and Y-axes, K_{2x} and K_{2y}, are respectively evaluated as[24]

$$K_{2x} = \frac{1}{\frac{L_t^3\left(L_t + L_{b1}\right)}{Ehw^3\left(4L_t + L_{b1}\right)} + \frac{L_{b2}}{Ehw}}, \tag{4}$$

$$K_{2y} = \frac{1}{\frac{L_{b1}^3\left(L_t + L_{b1}\right)}{Ehw^3\left(L_t + 4L_{b1}\right)} + \frac{L_{b2}^3}{4Ehw^3}}. \tag{5}$$

In the following section, we will use the above derived spring constants to evaluate cross-axis sensitivities.

3. Cross-axis Displacement Computation Model

3.1 Cross-axis displacement computation model for the inner spring system

The energy method is utilized to derive the equations for the spring constants. The free end of the springs is subjected to an applied force (or moment) in the desired direction, and the resulting displacement is calculated symbolically as a function of the design variables and applied force. Various boundary conditions are applied in these computations to account for different modes of deformation in the spring. When forces (or moments) act on the ends of the flexure, the total deformation energy U is evaluated as[25]

$$U = \sum_{beam\, i=1}^{N} \int_{0}^{L_i} \frac{M_i.(\xi)^2}{2.E.I_i} d\xi. \tag{6}$$

In Eq. (6), L_i denotes the length of the i-th beam in the flexure, M_i is the bending moment transmitted through the i-th beam, and Young's modulus of the structural material is represented by E, while I_i stands for the moment of inertia of the i-th beam about the pertinent axis. The bending moment can be described as a linear function of the applied forces and moments at the flexure's endpoints. The calculation for the displacement at any given direction of the flexure's endpoint, denoted as ζ, is expressed as

$$\delta\zeta = \frac{\partial U}{\partial F_\zeta}, \tag{7}$$

where F_ζ stands for the force exerted at the endpoint in a particular direction. Similarly, applied moments can be associated with angular displacements. Our aim here is to determine the displacement in a particular direction as a result of the applied force (or moment) in a different direction. Utilizing the boundary conditions, as depicted in Fig. 1(d) and Table 3, we derive a set of linear equations that incorporate the applied forces, moments, and the unknown displacement. Solving this equation set results in a linear connection between the displacement and the applied force, especially for the cross-axis spring constant in question. The spring constant is determined by the physical dimensions of the spring through the constant of proportionality. Similarly, we derive models for the out-of-plane cross-axis spring constants using a comparable method.

K_{xy} represents the elastic coupling between the translational modes x and y (applied force F_x, displacement $\delta_y \neq 0$). $K_{x\phi_z}$ denotes the elastic coupling between the translational mode x and the rotational mode ϕ_z (applied force F_x, displacement $\delta_{\phi_z} \neq 0$). $K_{y\phi_z}$ indicates the elastic coupling between the translational mode y and the rotational mode ϕ_z (applied force F_y, displacement $\delta_{\phi_z} \neq 0$). The analytical expression describing the elastic coupling between x, y, and modes for one spring in the U-shaped spring configuration is[26]

$$K_{xy} = \frac{9EI_{zb}I_{zt}\left(L_{b1} - L_{b2}\right)\left(2I_{zt}L_{b1}L_{b2} + I_{zb}\left(L_{b1} + L_{b2}\right)L_t\right)}{D}. \tag{8}$$

Table 3
Boundary conditions and equations solved for calculating spring constants.

Spring constant	Boundary conditions	Force/moment
K_{xy}	$\delta_x = 0$; $\delta_{\phi_z} = 0$	F_x
$K_{(x\phi_z)}$	$\delta_x = 0$; $\delta_y = 0$	F_x
$K_{(y\phi_z)}$	$\delta_x = 0$; $\delta_y = 0$	F_y

In Eq. (8), D is calculated as

$$D = L_t\left(3{I_{zt}}^2 L_{b1}L_{b2}\left(L_{b1}^3 + L_{b2}^3\right) + {I_{zb}}^2\left(L_{b1}^3 + L_{b2}^3\right){L_t}^2 + I_{zb}I_{zt}\left(L_{b1}^4 + 4L_{b1}^3L_{b2} + 3L_{b1}^2L_{b2}^2 + 4L_{b1}L_{b2}^3 + L_{b2}^4\right)L_t\right). \quad (9)$$

Here, I_{zb} and I_{zt} are the moments of inertia of the U-shaped spring about their individual z-axis and are calculated as

$$I_{zb} = I_{zt} = \frac{hw^3}{12}. \quad (10)$$

Manufacturing variations naturally occur as part of any fabrication process. $K_{x\phi_z}$ and $K_{y\phi_z}$ are caluculated as

$$K_{x\phi_z} = \frac{A}{D}, \quad (11)$$

$$K_{y\phi_z} = \frac{B}{D}. \quad (12)$$

In Eqs. (11) and (12), the expressions for calculated A and B are presented as follows:

$$\begin{aligned} A = -3EI_{zb}I_{zt}\Bigg(&\left(\left(I_{zt}\left(\left(L_{b1}^2 + L_{b2}^2\right)^2 + 4L_{b1}L_{b2}\left(L_{b1} - L_{b2}\right)^2\right)/L_t + 4I_{zb}\left(L_{b1}^3 + L_{b2}^2L_{b1}\right)\right)L_y\right. \\ &-\left(6I_{zt}L_{b1}^2L_{b2} + 6I_{zt}L_{b1}L_{b2}^2 - 3I_{zb}L_{b1}^2L_t + 3I_{zb}L_{b2}^2L_t\right)L_x \\ &\left.+I_{zt}\left(L_{b2}^4 + 3L_{b1}^2L_{b2}^2 - 2L_{b1}^3L_{b2}\right) - I_{zb}L_t\left(-L_{b1}^3 + 2L_{b1}L_{b2}^2 + 2L_{b2}^3\right)\right)\Bigg), \end{aligned} \quad (13)$$

$$\begin{aligned} B = 3EI_{zb}\Big(&I_{zt}\left(-6I_{zt}L_{b1}^2L_{b2} + 6I_{zt}L_{b1}L_{b2}^2 - 3I_{zb}L_{b1}^2L_t + 3I_{zb}L_{b2}^2L_t\right)L_y \\ &+\left(I_{zb}^2L_t^3 + 12I_{zt}^2L_{b1}L_{b2}L_t + 4I_{zb}I_{zt}L_{b1}L_t^2 + 4I_{zb}I_{zt}L_{b2}L_t^2\right)L_x \\ &+L_t\left(I_{zb}^2L_t^2L_{b1} + I_{zb}I_{zt}L_t\left(2L_{b1}^2 + 4L_{b1}L_{b2} + L_{b2}^2\right) + 6I_{zt}^2L_{b1}^2L_{b2}\right)\Big). \end{aligned} \quad (14)$$

Variations in spring beam widths can cause elastic cross-axis coupling. In MEMS fabrication processes, it is acknowledged that the geometric property can vary by up to 10% across a wafer.[26] Therefore, in the following analysis, we consider the variations in beam widths within individual springs.

The stiffness matrices for the component springs *TL*, *TR*, *BL*, and *BR* {*TL*, *TR*, *BL*, and *BR* represent spring K_2 at the top-left, top-right, bottom-left, and bottom-right positions, respectively, relative to mass M_2 [Fig. 1(a)]} are determined by[26]

$$K_{TL} = \begin{bmatrix} K_{xx} & -K_{xy} & K_{x\Phi_z} \\ -K_{xy} & K_{yy} & -K_{y\Phi_z} \\ K_{x\Phi_z} & -K_{y\Phi_z} & K_{\Phi_z\Phi_z} \end{bmatrix}, K_{TR} = \begin{bmatrix} K_{xx} & K_{xy} & K_{x\Phi_z} \\ K_{xy} & K_{yy} & K_{y\Phi_z} \\ K_{x\Phi_z} & K_{y\Phi_z} & K_{\Phi_z\Phi_z} \end{bmatrix}, \tag{15}$$

$$K_{BL} = \begin{bmatrix} K_{xx} & K_{xy} & -K_{x\Phi_z} \\ K_{xy} & K_{yy} & -K_{y\Phi_z} \\ -K_{x\Phi_z} & -K_{y\Phi_z} & K_{\Phi_z\Phi_z} \end{bmatrix}, K_{BR} = \begin{bmatrix} K_{xx} & -K_{xy} & -K_{x\Phi_z} \\ -K_{xy} & K_{yy} & K_{y\Phi_z} \\ -K_{x\Phi_z} & K_{y\Phi_z} & K_{\Phi_z\Phi_z} \end{bmatrix}. \tag{16}$$

The hypothetical beam width is assumed to be w in the absence of manufacturing errors. In the presence of manufacturing errors $w_1 = (1 + \Delta)$ depicted in Fig. 2, we can estimate the stiffness variation due to a fractional width adjustment Δ (where Δ represents the percentage

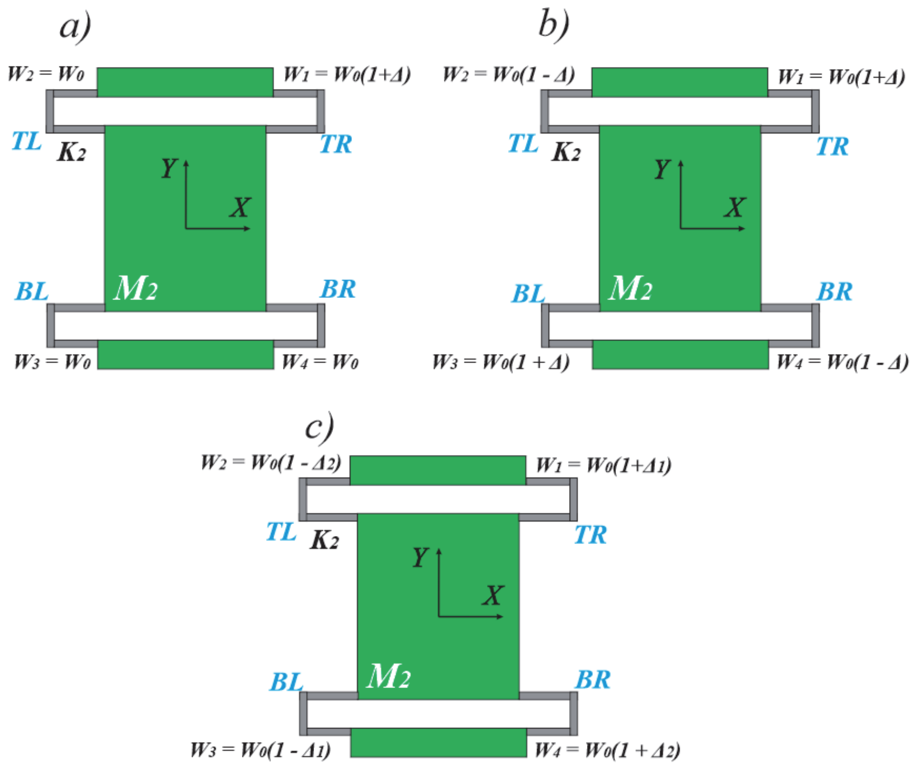

Fig. 2. (Color online) Sensor models with manufacturing error. (a) Case 1: only the *TR* spring is subject to Δ error, i.e., $\Delta_1 = \Delta$, $\Delta_2 = \Delta_3 = \Delta_4 = 0$. (b) Case 2: the *TR* and *BL* springs are subject to Δ error, while the *TL* and *BR* springs are subject to $-\Delta$ error, i.e., $\Delta_1 = \Delta_3 = \Delta$ and $\Delta_2 = \Delta_4 = -\Delta$. (c) Case 3: the springs *TL*, *TR*, *BL*, and *BR* are subject to the respective errors of $-\Delta_2$, Δ_1, $-\Delta_1$, and Δ_2 (i.e., $\Delta_2 + \Delta_4 = 0$, $\Delta_1 + \Delta_3 = 0$, and $\Delta_1 \neq \Delta_2$).

error of the width) with the knowledge that stiffness is proportional to w^3. In the presence of a slight fractional alteration Δ in width, we can approximate the fractional variation in the initial stiffness of a single spring K_0 using a factor of 3Δ. The spring stiffness due to manufacturing errors, K', is calculated as $K' = K_0(1 + 3\Delta)$. Therefore, the in-plane segment of the stiffness matrix can be expressed as[26]

$$K = 3\begin{bmatrix} \frac{4}{3K_{xx}} & K_{xy}\left(\Delta_1+\Delta_3-\Delta_2-\Delta_4\right) & K_{x\Phi_z}\left(\Delta_1-\Delta_3+\Delta_2-\Delta_4\right) \\ K_{xy}\left(\Delta_1+\Delta_3-\Delta_2-\Delta_4\right) & \frac{4}{3K_{yy}} & K_{y\Phi_z}\left(\Delta_1-\Delta_3-\Delta_2+\Delta_4\right) \\ K_{x\Phi_z}\left(\Delta_1-\Delta_3+\Delta_2-\Delta_4\right) & K_{y\Phi_z}\left(\Delta_1-\Delta_3-\Delta_2+\Delta_4\right) & \frac{4}{3K_{\Phi_z\Phi_z}} \end{bmatrix}. \tag{17}$$

Here, Δ_1, Δ_2, Δ_3, and Δ_4 represent manufacturing errors on the *TR*, *TL*, *BL*, and *BR* springs, respectively.

Here, we study three cases of manufacturing errors related to U-shaped springs. The first two cases are shown in Fig. 2, where Fig. 2(a) shows the sensor model with the manufacturing error Δ arising only in the *TR* spring, i.e., $\Delta_1 = \Delta$, $\Delta_2 = \Delta_3 = \Delta_4 = 0$ (case 1), while Fig. 2(b) shows the sensor model with the manufacturing errors Δ arising in the *TR* and *BL* springs and $-\Delta$ in the *TL* and *BR* springs, i.e., $\Delta_1 = \Delta_3 = \Delta$ and $\Delta_2 = \Delta_4 = -\Delta$. (case 2).

Starting from Eq. (17), we have the stiffness matrix of the spring in cases 1 and 2 as

$$K_{T1} = \begin{bmatrix} 4K_{xx} & 3K_{xy}\Delta & 3K_{x\phi_z}\Delta \\ 3K_{xy}\Delta & 4K_{yy} & 3K_{y\phi_z}\Delta \\ 3K_{x\phi_z}\Delta & 3K_{y\phi_z}\Delta & 4K_{\phi_z\phi_z} \end{bmatrix}, \tag{18}$$

$$K_{T2} = \begin{bmatrix} 4K_{xx} & K_{xy}\left(12\Delta\right) & 0 \\ K_{xy}\left(12\Delta\right) & 4K_{yy} & 0 \\ 0 & 0 & 4K_{\Phi_z\Phi_z} \end{bmatrix}, \tag{19}$$

where K_{T1} and K_{T2} are the stiffness matrices of the U-shaped spring in cases 1 and 2, respectively. The third case of investigation is shown in Fig. 2(c). Here, the springs *TL*, *TR*, *BL*, and *BR* are subject to the respective errors of $-\Delta_2$, Δ_1, $-\Delta_1$, and Δ_2, (i.e., $\Delta_2 + \Delta_4 = 0$, $\Delta_1 + \Delta_3 = 0$, and $\Delta_1 \neq \Delta_2$). Derived from Eq. (17), we have the stiffness matrix of the spring in the third case as

$$K_{T3} = 3\begin{bmatrix} \frac{4}{3}K_{xx} & 0 & K_{x\Phi_z}2(\Delta_1 - \Delta_2) \\ 0 & \frac{4}{3}K_{yy} & K_{y\Phi_z}2(\Delta_1 + \Delta_2) \\ K_{x\Phi_z}2(\Delta_1 - \Delta_2) & K_{y\Phi_z}2(\Delta_1 + \Delta_2) & \frac{4}{3}K_{\Phi_z\Phi_z} \end{bmatrix}. \tag{20}$$

Here, K_{T3} is the stiffness matrix of the U-shaped spring in case 3. The relationship among force, displacement, and system stiffness is[25]

$$\begin{bmatrix} F_x \\ F_y \\ M_{\Phi_z} \end{bmatrix} = K\begin{bmatrix} x \\ y \\ \Phi_z \end{bmatrix}. \tag{21}$$

We consider case 1:

$$\begin{bmatrix} F_x \\ F_y \\ M_{\Phi_z} \end{bmatrix} = \begin{bmatrix} 4K_{xx} & 3K_{xy}\Delta & 3K_{x\phi_z}\Delta \\ 3K_{xy}\Delta & 4K_{yy} & 3K_{y\phi_z}\Delta \\ 3K_{x\phi_z}\Delta & 3K_{y\phi_z}\Delta & 4K_{\phi_z\phi_z} \end{bmatrix}\begin{bmatrix} x \\ y \\ \Phi_z \end{bmatrix}. \tag{22}$$

From the above system of equations, it can be inferred that

$$\begin{aligned} F_x &= 4K_{xx}x + 3K_{xy}\Delta y + 3K_{x\phi_z}\Delta\Phi_z, \\ F_y &= 3xK_{xy}\Delta + 4yK_{yy} + 3yK_{y\phi_z}\Delta, \\ M_{\Phi_z} &= 3xK_{x\phi_z}\Delta + 3yK_{y\phi_z}\Delta + 4\Phi_z K_{\phi_z\phi_z}. \end{aligned} \tag{23}$$

When there is no force in the y-direction, the ratio of y displacement to x displacement $|y/x|$ in case 1 ($Y_{car\text{-}1}$) is given as

$$Y_{car\text{-}1} = \left|\frac{y}{x}\right| = \frac{3}{4}\frac{K_{xy}\Delta}{K_{yy}} = \frac{3K_{xy}\Delta}{K_{2y}}. \tag{24}$$

In case 2, the analysis is similar. $Y_{car\text{-}2}$ is therefore derived as

$$Y_{car\text{-}2} = \left|\frac{y}{x}\right| = 3\frac{K_{xy}\Delta}{K_{yy}} = \frac{12K_{xy}\Delta}{K_{2y}}. \tag{25}$$

In case 3, there exists no direct coupling between the two in-plane translational modes x and y. However, there is a second-order coupling through the rotational mode. The mode x initially couples to the rotational mode Φ_z, which subsequently couples to the mode y. Therefore, the ratio of y displacement to x displacement in this case (Y_{car-3}) is calculated as

$$Y_{car\text{-}3} = \left|\frac{y}{x}\right| = \frac{\left(\sum K_{x\Phi_z i}\right)\left(\sum K_{y\Phi_z i}\right)}{\left(\sum K_{yyi}\right)\left(\sum K_{\Phi_z\Phi_z i}\right)}, \tag{26}$$

where $K_{\Phi_z\Phi_z i} = K_{xxi}L_2^2 + K_{yyi}W_2^2$.

3.2 Cross-axis displacement computation model for the outer spring system

Figure 3 shows the model of the sensor with the total proof mass ($M_1 + M_2$) suspended by four folded springs; the symbols of the springs are shown in the figure. We assume that the fabrication error of the spring on the right corner is denoted as Δ_F. L_y represents the distance between two springs along the Y-axis, and L_x is calculated as the width of the proof mass along the X-axis.

The stiffness matrix of the entire system is calculated as[27]

$$K' = \begin{bmatrix} 4K_{xx} & 0 & 3K_{x\phi_z}\Delta_F \\ 0 & 4K_{yy} & 3K_{y\phi_z}\Delta_F \\ 3K_{x\phi_z}\Delta_F & 3K_{y\phi_z}\Delta_F & 4K_{\phi_z\phi_z} \end{bmatrix}. \tag{27}$$

The ratio (X_{car}) of x displacement to y displacement (referring to Fig. 4) when there is no force in the x-direction is given by

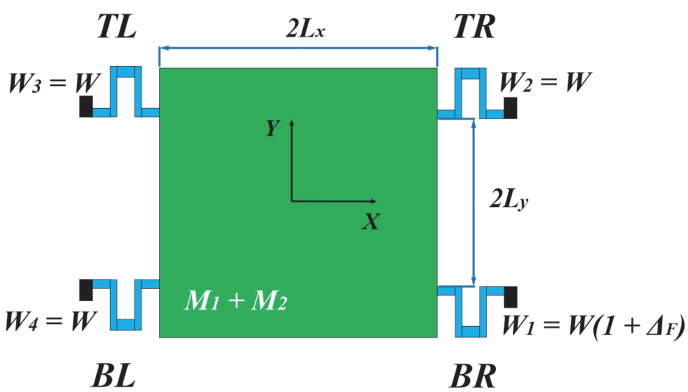

Fig. 3. (Color online) X-axis acceleration sensing sensor model with the total proof mass ($M_1 + M_2$) taking into account the effect of fabrication error (ΔF) on the width of the spring beam.

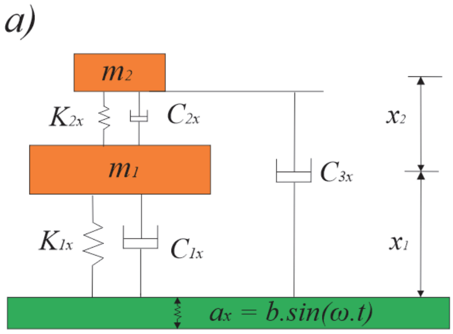

Fig. 4. (Color online) (a) Oscillation model of the sensor along the *X*-axis. (b) Oscillation model of the sensor along the *Y*-axis.

$$X_{car} = \frac{x}{y} = \frac{\left(\sum K_{x\Phi_z i}\right)\left(\sum K_{y\Phi_z i}\right)}{\left(\sum K_{xxi}\right)\left(\sum K_{\Phi_z\Phi_z i}\right)}, \tag{28}$$

where

$$K_{x\Phi_z i} = K_{xxi}L_y,\ K_{y\Phi_z i} = K_{yyi}L_x, \text{ and } K_{\Phi_z\Phi_z i} = K_{xxi}L_y^2 + K_{yyi}L_x^2. \tag{29}$$

For the folded spring, we have $K_{yyi} \gg K_{xxi}$, so $K_{\Phi_z\Phi_z i} = K_{yyi}L_x^2$.

Substituting the values of $(\sum K_{x\Phi_z i})$ and $(\sum K_{y\Phi_z i})$ from Eq. (27) into Eq. (28), we obtain

$$X_{car} = \frac{x}{y} = \frac{\left(3K_{x\phi_z}\Delta_F\right)\left(3K_{y\phi_z}\Delta_F\right)}{\left(\sum K_{xxi}\right)\left(\sum K_{\Phi_z\Phi_z i}\right)}. \tag{30}$$

Substituting the values of $K_{x\phi_z}$ and $K_{y\phi_z}$ from Eq. (29) into Eq. (30), we obtain

$$X_{car} = \frac{\left(3K_{xx}L_y\Delta_F\right)\left(3K_{yy}L_x\Delta_F\right)}{\left(4K_{xx}\right)\left(4K_{yy}L_x^2\right)} = \frac{9L_y\Delta_F^2}{16L_x}. \tag{31}$$

In this case, X_{car} depends on the distance ratio (L_y/L_x) and is quadratically proportional to Δ_F.

4. Acceleration Model Excited along the *X*- and *Y*-axes and Sensitivity of the Sensor

Now, we consider the sensor excited by the input accelerations $a_x = b\sin(\omega t)$ along the *X*- axis and $a_y = a\sin(\omega t)$ along the *Y*-axis, as shown in Fig. 1(a). Here, the amplitudes *a* and *b* of a_x and a_y are set at the same value of 9.8 m/s^2. The oscillation models of the sensor along the *X*- and

Y-axes are shown in Figs. 4(a) and 4(b), respectively. The parameters denoted in Fig. 4 are explained as follows: m_1 is the mass of the outer frame of the sensor M_l, m_2 is the proof mass inside the sensor M_2, K_{1x} and K_{1y} are the stiffnesses of spring K_1 in the X- and Y-axis directions, K_{2x} and K_{2y} are the stiffnesses of spring K_2 in the X- and Y-axis directions, C_{1x} and C_{1y} are the damping coefficients of M_1 relative to the base along the X- and Y-axes, and C_{2x} and C_{2y} are the damping coefficients of M_2 relative to M_1 along the X- and Y-axes, respectively. In addition, C_{3x} and C_{3y} are the damping coefficients of M_2 relative to the base along the X- and Y-axes, respectively. In general, when ignoring the direction of oscillation, we have the following amplitudes of frame M_1 and mass M_2.[28]

$$\begin{bmatrix} -m_1\omega^2 + c_1 j\omega + k_1 & c_3 j\omega - m_2\omega^2 \\ -\left(k_2 + c_2 j\omega\right) & -m_2\omega^2 + \left(c_3 + c_2\right) j\omega + k_2 \end{bmatrix} \begin{bmatrix} A_1 \\ A_2 \end{bmatrix} = \begin{bmatrix} m_1 a + m_2 a \\ m_2 a \end{bmatrix} \tag{32}$$

Here, A_1 is the amplitude of frame M_1; A_1 is the amplitude of mass M_2; a represents the amplitude of the input acceleration; c_1, c_2, and c_3 and k_1 and k_2 are damping coefficients and spring constants, respectively. When considering oscillation in the X-direction, the coefficients c_1, c_2, and c_3, the constants k_1 and k_2, and input acceleration take the values c_{1x}, c_{2x}, and c_{3x}, k_{1x} and k_{2x}, and b, respectively. At that time, the oscillation amplitudes in the X-direction of M_1 and M_2 are $A_{m1\text{-}x}$ and $A_{m2\text{-}x}$, respectively. Similarly, while analyzing the oscillation in the Y-direction, with the damping coefficients, spring constants, and input acceleration being c_{1y}, c_{2y}, and c_{3y}, k_{1y} and k_{2y}, and a, respectively, the oscillation amplitudes of M_1 and M_2 are $A_{m1\text{-}y}$ and $A_{m2\text{-}y}$, respectively.

If the sensor oscillates in the X-direction, a displacement will be induced in the Y-direction, Y_{cad}, evaluated as

$$Y_{Cad\text{-}1,2,3} = A_{m2\text{-}x} Y_{car\text{-}1,2,3}. \tag{33}$$

The oscillation of the sensor in the Y-direction leads to a displacement in the X-direction, X_{Cad}, evaluated as

$$X_{Cad} = A_{m1\text{-}y} X_{car}. \tag{34}$$

To calculate the damping coefficients C_{ix} and C_{iy}, we consider air damping to be the dominant damping mechanism in the sensor. Air damping consists of two main components: slide film air damping and squeeze film air damping. In the case of slide film air damping, the gap distance (distance from the proof mass and the frame to the substrate), denoted as d_t, is significantly smaller than δ (the effective decay distance $\delta = \sqrt{2\mu / \rho\omega}$, in which ρ is the density of air, μ is the coefficient of viscosity of air, and ω is the frequency of the sensor). The damping coefficients of slide film air damping force at the bottom can be calculated using the Couette-flow-type model as[29]

$$C_{Couette\text{-}flow} = \mu \frac{A_q}{d_t}, \tag{35}$$

where A_q is the surface area of the moving objects, mass proof, and frame. In a scenario where the moving structure is situated far from any objects positioned above it, the damping force acting on the moving parts follows a Stokes-flow pattern. The corresponding damping coefficient is described as

$$C_{Stokes\text{-}flow} = \mu \frac{A_q}{\delta}. \tag{36}$$

The assessment of the air drag force on the moving mass M_2 and the moving frame M_1 is complex. Therefore, an approximation of its damping coefficient is given by[29]

$$C_{Drag\,force} = \frac{32}{3} \mu l. \tag{37}$$

Here, l represents the characteristic dimension of the moving structure, which may be considered as half the width of the proof mass. In the case of squeeze film air damping, the coefficient of damping force for the rectangular fingers, $C_{squeeze}$, is calculated as[29]

$$C_{squeeze} = \frac{\mu B^3 L_s N_s}{d_0^3}, \tag{38}$$

where d_0, L_s, B, and N_s represent the gap distance, overlapping finger length, finger width, and the number of comb fingers of the sensing combs in the *X*- and *Y*-directions, respectively.

Therefore, the total damping coefficient is derived using Eqs. (35)–(38) as

$$C_{total} = \mu \frac{A_q}{d_t} + \mu \frac{A_q}{\delta} + \mu l \frac{32}{3} + \frac{\mu B^3 L_s}{d_0^3} N_s. \tag{39}$$

Applying the above formula to the outer frame M_1 and inner mass M_2, we obtain the following calculation formulas for the damping coefficients C_{ix} and C_{iy}:

$$
\begin{aligned}
C_{1x} &= \mu\frac{A_{q1}}{d_t}+\mu\frac{A_{q1}}{\delta}+\mu\frac{L_1}{2}\frac{32}{3}+\frac{\mu B_1^3 L_1}{d_1^3}N_1,\\
C_{1y} &= \mu\frac{A_{q1}}{d_t}+\mu\frac{A_{q1}}{\delta}+\mu\frac{L_1}{2}\frac{32}{3},\\
C_{3x} &= \mu\frac{A_{q2}}{d_t}+\mu\frac{A_{q2}}{\delta}+\mu\frac{L_2}{2}\frac{32}{3},\\
C_{3y} &= \mu\frac{A_{q2}}{d_t}+\mu\frac{A_{q2}}{\delta}+\mu\frac{W_2}{2}\frac{32}{3},\\
C_{2y} &= \frac{\mu B_2^3 L_2}{d_2^3}N_2,\\
C_{2x} &= 0\,\mathrm{Ns/m},
\end{aligned}
\tag{40}
$$

where A_{q1} is the surface area of the outer frame M_1 and A_{q2} is the surface area of the proof mass M_2.

To derive the sensitivity of the sensor, we start by determining the variation in sensing capacitance under changing displacement in each motion direction. The static sensing capacitance of the sensor in the X-direction is given by $C_1 = C_2 = N_1\varepsilon L_1 B_1/d$.[30] Here, ε represents the dielectric constant of air. C_1 and C_2 respectively represent the upper and bottom comb capacitances in Fig. 1(a). When an acceleration $a\sin(\omega t)$ is applied in the X-direction, the proof mass undergoes a displacement x. The change in capacitance is derived as

$$
C_1 = \frac{\varepsilon L_1 B_1 N_1}{d_1 - x} \text{ and } C_2 = \frac{\varepsilon L_1 B_1 N_1}{d_1 + x}. \tag{41}
$$

Hence, the differential change in capacitance can be expressed as

$$
\Delta C = C_1 - C_2 = \frac{2\varepsilon L_1 B_1 N_1 x}{d_1^2 - x^2}. \tag{42}
$$

The differential change in capacitance in the Y-direction is derived by following the same procedure as in the X-direction described above. In this case, C_1 and C_2 respectively represent the left and right comb capacitances in Fig. 1(a). The common electrode for the movable comb fingers is denoted as V_G. The electrode pads on the left and on the right are for supplying voltages ($V_{s+,y}$, $V_{s-,y}$) to the remaining ends of the differential capacitance for sensing acceleration along the Y-direction, while $V_{s+,x}$ and $V_{s-,x}$ are supplied to the top and bottom fixed comb electrodes of the differential capacitance for sensing acceleration along the X-direction.

The accelerometer's sensitivity, often called its scale factor, refers to the ratio of the sensor's electrical response to the detected mechanical input. The formula for sensitivity is expressed as

$$S_x = \frac{\Delta C_x}{b}; S_y = \frac{\Delta C_y}{a}; S_{xc} = \frac{\Delta C_{x\text{-}cross}}{a}; S_{yc} = \frac{\Delta C_{y\text{-}cross}}{b}. \tag{43}$$

Here, S_x represents the sensitivity of the sensor along the X-axis, S_y represents the sensitivity along the Y-axis, S_{xc} denotes the sensitivity caused by cross-axis effects on the X-axis when an input acceleration (a) is applied along the Y-axis, and S_{yc} denotes the sensitivity caused by cross-axis effects on the Y-axis when an input acceleration (b) is applied along the X-axis. In this context, ΔC_x and ΔC_y represent the changes in the capacitances of the outer and inner sensing comb fingers, respectively. Moreover, $\Delta C_{x\text{-}cross}$ and $\Delta C_{y\text{-}cross}$ represent the impacts of cross-axis effects on the outer and inner sensing comb fingers, respectively.

5. Results and Discussion

5.1 Relationship between spring stiffness K_1 values in X- and Y-directions

Figure 5(a) presents the stiffness ratios in the Y- and X-directions of the folded spring system, K_{1y}/K_{1x}, investigated as a function of l_{kb}/l_{ka} for various w_{kb}/w_{ka} values. Thus, K_{1y}/K_{1x} primarily

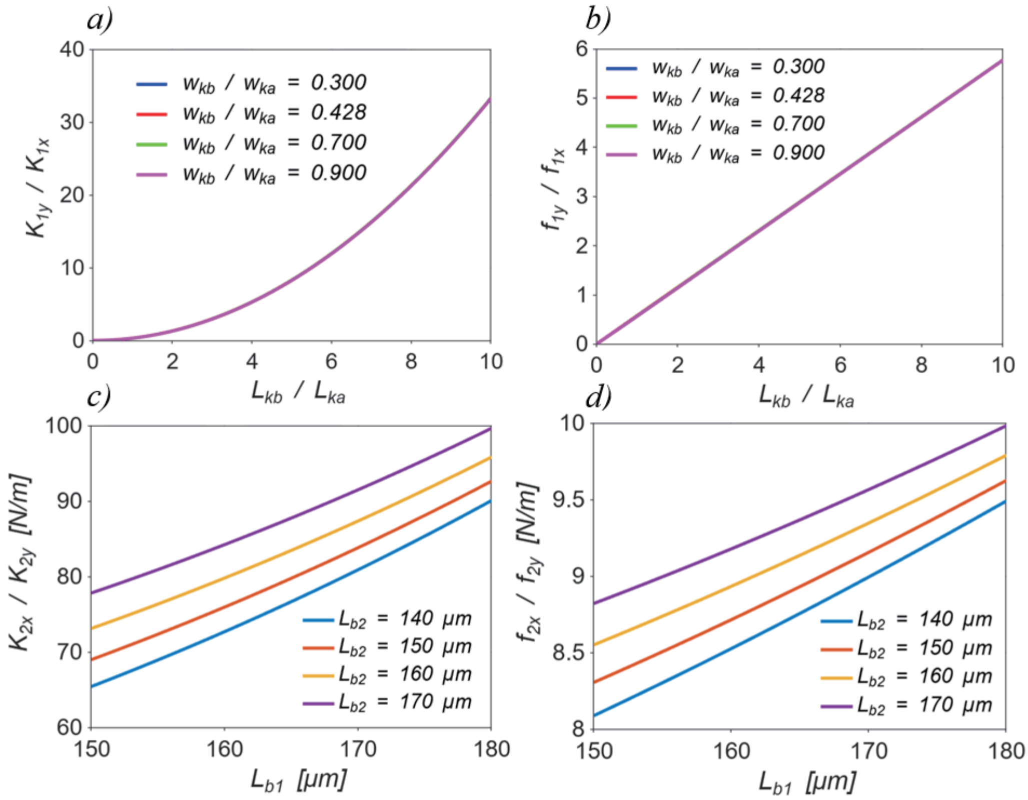

Fig. 5. (Color online) (a) Stiffness ratios in the Y- and X-directions of the folded spring system, K_{1y}/K_{1x}, investigated as a function of l_{kb}/l_{ka} with various w_{kb}/w_{ka} values. (b) Frequency f_{1y}/f_{1x} ratios in the Y- and X-directions of frame M_1 investigated as a function of l_{kb}/l_{ka} with various w_{kb}/w_{ka} values. (c) Stiffness ratios in the Y- and X-directions of the U-shaped spring system, K_{2x}/K_{2y}, investigated as a function of L_{b1} with various L_{b2} values. (d) Frequency f_{2x}/f_{2y} ratios in the Y- and X-directions of proof mass M_2 investigated as a function of $L_{b1}$with various L_{b2} values.

depends on l_{kb}/l_{ka} and is less affected by the w_{kb}/w_{ka} ratio. In a practical design, a high K_{1y}/K_{1x} value is required so that the stiffness in the Y-direction is significantly greater than that in the X-direction in order to prioritize the oscillation along the X-axis and limit the oscillation along the Y-axis for the outer frame M_1. With $w_{kb}/w_{ka} = 0.428$ and $l_{kb}/l_{ka} = 4.57$, K_{1y}/K_{1x} is obtained to be 6.96. Therefore, we can increase l_{kb} and decrease l_{ka} to achieve a higher K_{1y}/K_{1x} ratio, which is preferable for optimizing the system. In Fig. 5(b), it is shown that at w_{kb}/w_{ka} =0.428 and $l_{kb}/l_{ka} = 4.57$, f_{1y}/f_{1x} takes the value of 2.61. When f_{1y}/f_{1x} is large, decoupling the two modes of oscillation in the X- and Y-directions of M_1 becomes effective.[31,32]

Figure 5(c) presents the stiffness ratios in the Y- and X-directions of the U-shaped spring system, K_{2x}/K_{2y}, investigated as a function of L_{b1} with various L_{b2} values. We can see that K_{2x}/K_{2y} increases with L_{b1}. In addition, for the same value of L_{b1}, when L_{b2} decreases, K_{2x}/K_{2y} also decreases. When L_{b1} = 170 µm and L_{b2} = 160 µm, K_{2x}/K_{2y} takes the value of 87.37. This value ensures the stiffness of spring K_2 in the X-direction and the flexibility in the Y-direction when the sensor is in operation. Figure 5(d) presents the frequency f_{2x}/f_{2y} in the Y- and X-directions of the proof mass M_2 investigated as a function of L_{b1} with various L_{b1} values. The relationship of f_{2x}/f_{2y} with L_{b1} and L_{b2} is similar to that of K_{2x}/K_{2y} with the investigated parameter ranges. These results indicate that the f_{2x}/f_{2y} ratio is higher than 8.1 for $L_{b1} \geq 150$ µm, which leads to the complete decoupling of the oscillations of the mass M_2 in the X- and Y-directions.[18,33]

5.2 Oscillation amplitudes of frame M_1 and proof mass M_2

Figures 6(a) and 6(b) respectively present the relationships of the oscillation amplitudes of the frame $M_1(Y_1)$ and proof mass $M_2(Y_2)$ with the frequency of the input acceleration along the Y-direction. Thus, when the spring stiffness K_{1y} increases, the oscillation amplitude of the frame M_1 decreases [Fig. 6(a)]. Similarly, when the spring stiffness K_{2y} increases, the oscillation amplitude of the proof mass M_2 also decreases [Fig. 6(b)]. In this study, we use the values K_{1y} = 35989 N/m and K_{2y} = 1417 N/m by using the spring parameters in Table 2. At K_{1y} = 35989

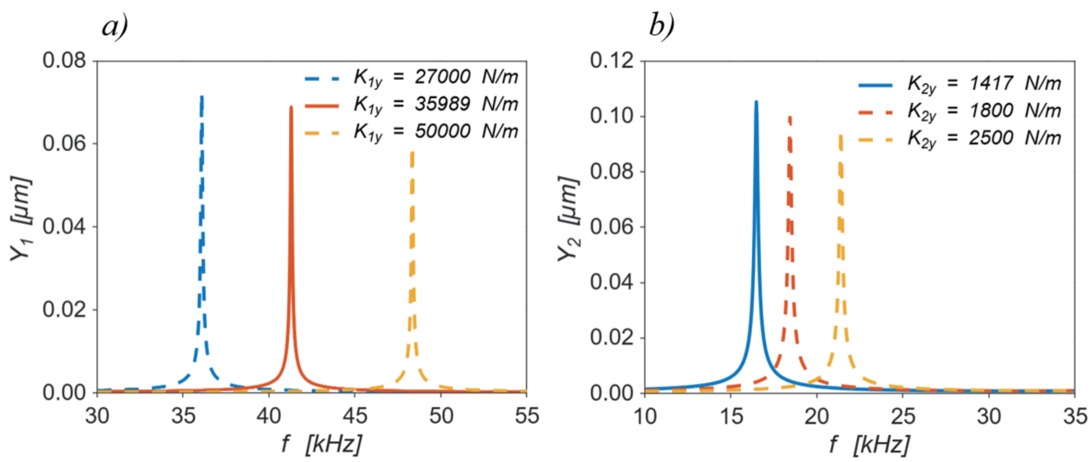

Fig. 6. (Color online) (a) Oscillation amplitudes of frame M_1 along the Y-axis (motion relative to the ground). (b) Oscillation amplitudes of proof mass M_2 along the Y-axis (motion relative to frame M_1) with input acceleration a = 1g (g is the value of gravitational acceleration).

N/m and K_{2y} = 1417 N/m, we obtain the corresponding amplitudes of Y_1 = 0.067 μm in Fig. 6(a) and Y_2 = 0.105 μm in Fig. 6(b).

Figures 7(a) and 7(b) show the relationship between the oscillation amplitude of the frame $M_1(X_1)$ and the proof mass $M_2(X_2)$ with the frequency of the input acceleration. In Fig. 7(a), we observe that as the stiffness of spring K_1 in the X direction decreases, X_1 increases. Similarly, this also occurs with X_2 of the proof mass M_2 with different values of the stiffness of spring K_2 in the X-direction. From Figs. 7(a) and 7(b), we see that X_1 and X_2 take the values of 0.211 μm and 1.63 nm corresponding to the values K_{1x} = 5167 N/m and K_{2x} = 123805 N/m, respectively. The stiffness of spring K_1 in the X direction, K_{1x} = 5167 N/m, and the stiffness of spring K_2 in the X direction, K_{2x} = 123805 N/m, are calculated using Eqs. (1)–(5) with the parameter set of the spring shown in Table 2. In the above investigations, we used the damping coefficients $C_{1x} = 3.55 \times 10^{-4}$ Ns/m, $C_{1y} = 1.412 \times 10^{-4}$ Ns/m, $C_{3x} = 3.191 \times 10^{-5}$ Ns/m, $C_{2y} = 1.082 \times 10^{-4}$ Ns/m, and $C_{3y} = C_{3x}$ calculated using Eq. (40) with the parameters of the sensor shown in Table 1.

Now, we will consider the quality factor (Q) of the sensor. The Q values of the sensor in the X-direction (Q_x) and Y-direction (Q_y) are calculated using the expressions $Q_x = m_{1s}2\pi f_{1x}/C_{1x}$ and $Q_y = m_{2s}2\pi f_{2y}/C_{2y}$,[34] where $m_{1s} = 5.6852 \times 10^{-7}$ (kg) is the mass of M_1 and the outer sensing comb fingers, and $m_{2s} = 1.4632 \times 10^{-7}$ (kg) is the mass of M_2 and the inner sensing comb fingers. In addition, f_{1x} = 13.804 (kHz) and f_{2y} = 16.464 (kHz) are the resonance frequencies of M_1 and M_2 when M_1 oscillates in the X-direction and M_2 oscillates in the Y-direction, respectively. The values of f_{1x} and f_{2y} are determined from Figs. 7(a) and 6(b). C_{1x}(= 3.55×10^{-4} Ns/m) and C_{2y}(= 1.082×10^{-4} Ns/m) are the damping coefficients whose values are determined in Sect. 5.2. Thus, Q_x and Q_y are calculated to be 138.9 and 139.9, respectively. The Q_x and Q_y values in the present study are similar to those in other high-sensitivity accelerometer designs.[35,36] The sensor's Q value can be adjusted by varying its design parameters such as spring stiffness, mass, and damping.

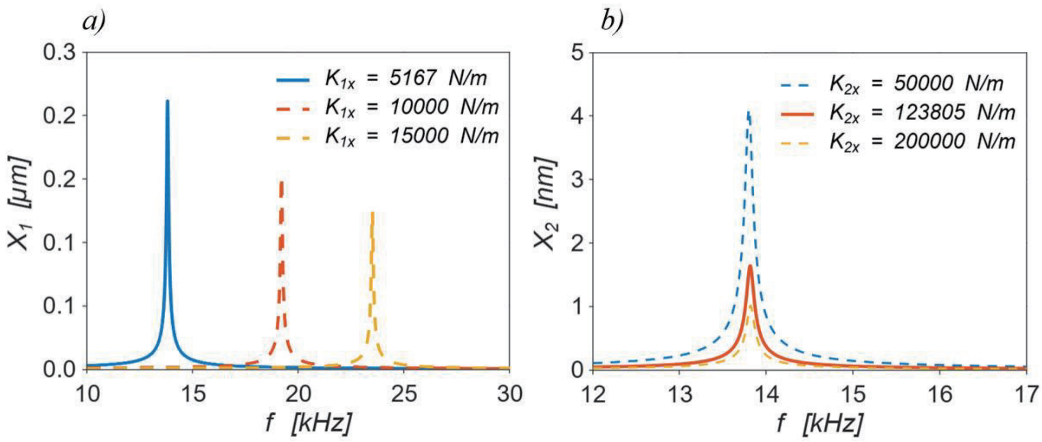

Fig. 7. (Color online) (a) Oscillation amplitude of the frame M_1 along the X-axis (relative motion to the ground). (b) Oscillation amplitude of the proof mass M_2 along the X-axis (motion relative to frame M_1) with input acceleration a = 1g (g is the value of the gravitational acceleration).

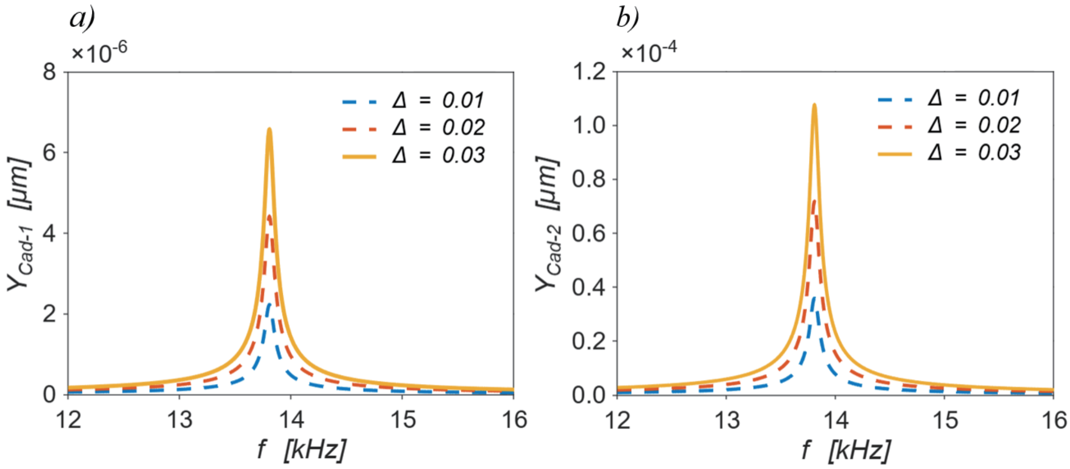

Fig. 8. (Color online) (a) Dependence of $Y_{Cad\text{-}1}$ on frequency with different values of the U-spring beam width error Δ in case 1. (b) Dependence of $Y_{Cad\text{-}2}$ on frequency with different values of the U-shaped spring beam width error Δ in case 2.

5.3 *Y*-cross-axis displacement in three cases ($Y_{Cad\text{-}1,2,3}$) and *X*-cross-axis displacement (X_{cad})

The dependence of $Y_{Cad\text{-}1}$ is investigated as a function of frequency with different values of the U-spring beam width error Δ in cases 1 and 2, and the results are shown in Fig. 8. From Fig. 8(a), we can see that as the error of the spring beam increases from 0.01 to 0.03, the Y-cross-axis displacement in case 1 ($Y_{Cad\text{-}1}$) also increases proportionately. At Δ = 0.03, $Y_{Cad\text{-}1} = 6.6 \times 10^{-6}$ µm.

The relationship between Δ and *Y*-cross-axis displacement in Fig. 8(b) is similar to that in Fig. 8(a). At Δ = 0.03, $Y_{Cad\text{-}2} = 1.1 \times 10^{-4}$ µm. Thus, the *Y*-cross-axis displacement in case 2 ($Y_{Cad\text{-}2}$) is 16.6 times larger than that in case 1 ($Y_{Cad\text{-}1}$).

Figure 9(a) shows $Y_{Cad\text{-}3}$ investigated as a function of frequency for different values of the U-shaped spring beam width error Δ_2 in case 3, keeping error Δ_1 (= 0.04) constant. The dependence of $Y_{Cad\text{-}3}$ on frequency and Δ_2 is similar to those in Figs. 8(a) and 8(b). However, with the same error values, the magnitude of $Y_{Cad\text{-}3}$ is tens times lower than those of $Y_{Cad\text{-}1}$ and $Y_{Cad\text{-}2}$. For example, at $\Delta_2 = 0.01$ (which matches the designed spring beam width of 10 µm with a fabrication error of 0.1 µm), $Y_{Cad\text{-}3}$ reaches a fabrication-error-induced displacement value of 5.2×10^{-7} µm, which is 211 times lower than that of $Y_{Cad\text{-}2}$ (1.1×10^{-4} µm). Moreover, from Fig. 9(b), we can see that when the beam width error Δ_F increases from 0.01 to 0.03, corresponding to fabrication errors in the spring beam width of 1, 2, and 3%, X_{Cad} increases markedly. At $\Delta_F = 0.03$ (corresponding to a designed beam width of 15 µm with a fabrication error of 0.45 µm), X_{Cad} is 3.2×10^{-5} µm. In this study, from the values presented above, we used the fabrication errors suitable for the present fabrication conditions.

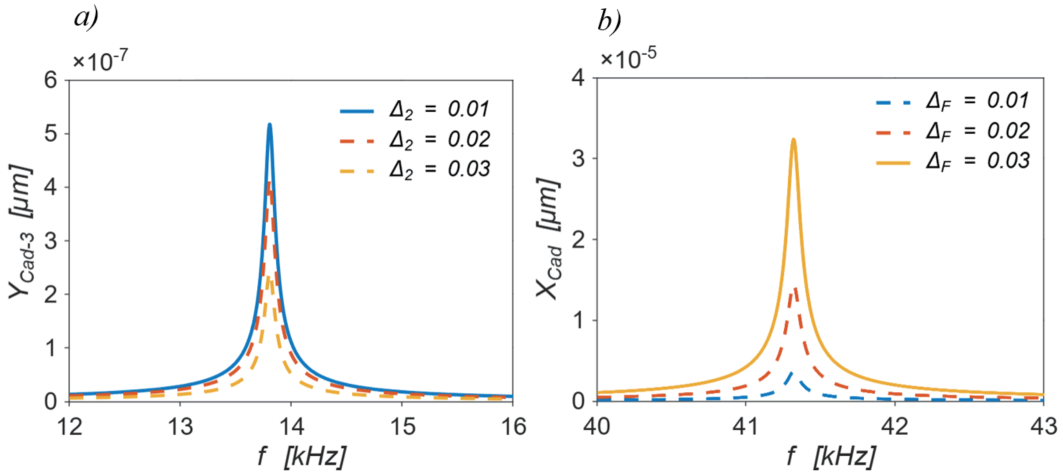

Fig. 9. (Color online) (a) Dependence of $Y_{Cad\text{-}3}$ on frequency with different values of the U-spring beam width error Δ in case 3. (b) Dependence of X_{Cad} on frequency with different values of the folded spring beam width error Δ_F; here, L_y/L_x=0.94.

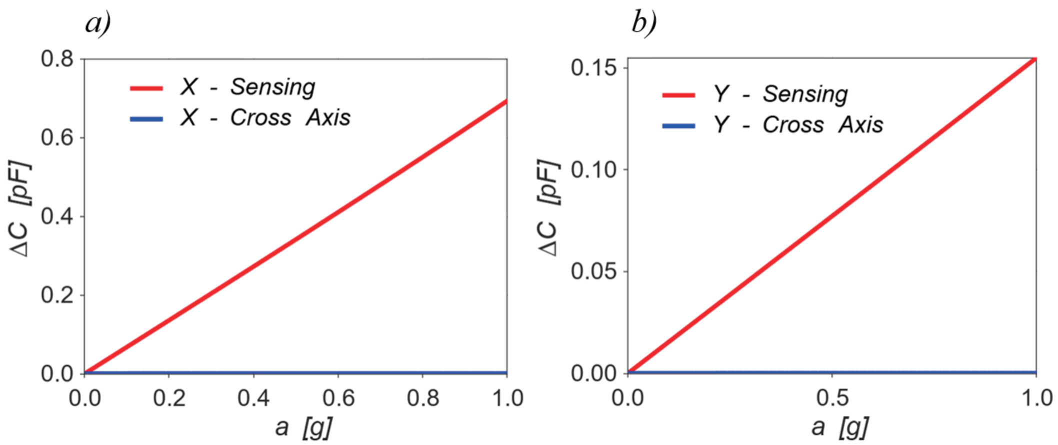

Fig. 10. (Color online) (a) Relationship between the variation in sensing capacitance Δ*C* and input acceleration for the *X*-axis and *X*-cross-axis sensitivities. (b) Relationship between the variation in sensing capacitance Δ*C* and input acceleration for the *Y*-axis and *Y*-cross-axis sensitivities in case 2 in which the fabrication-error-induced displacement is the largest.

5.4 Cross-axis sensitivities

Figure 10(a) presents the relationship between S_x and S_{xc} for different values of the input acceleration. Here, the input acceleration is measured in units of the gravitational acceleration (g). Although the *X*-axis sensitivity exhibits a linear relationship with the input acceleration and achieves a high value, S_x = 0.693 pF/g, the $X_{Cross\text{-}Axis}$ sensitivity conversely achieves a much lower value, S_{xc} = 0.0001 pF/g. At an acceleration of a = 1g and with a fabrication error of 0.45 μm in the beam width (Δ_F = 0.03 = 3%), S_{xc}/S_x = 0.0001(pF/g)/0.693(pF/g) = 0.014%. Figure 10(b) also shows low cross-axis sensitivity in the *Y*-direction. On the basis of the results of the analysis in Sect. 5.3, among the three cases of *Y*-cross-axis displacement errors, case 2 has the most significant impact. Therefore, we will use the results from this case to calculate the effect of input acceleration on capacitance variation. With a fabrication error of 0.1 μm in the beam width (Δ_2 = 1%) in case 2 and a = 1g, $S_{yc}/S_y = 1.3 \times 10^{-4}$ (pF/g)/0.154(pF/g) = 0.08%. In contrast to earlier studies, the cross-axis value found in our research is notably reduced. For example, in automotive airbag systems, accelerometers typically have a range of ± 50 g with a cross-axis sensitivity lower than 5%. However, for navigation applications, the required range is around ±1 g, with cross-axis sensitivities less than 0.1%.[37,38]

6. Conclusion

We presented a model of a two-axis accelerometer with minimized cross-axis sensitivity by using folded spring systems and optimizing their sizes. A theoretical model was established for comprehensively investigating the operation characteristics of the sensor, such as the operation frequency, the amplitude of oscillation, sensitivity, and cross-axis sensitivity depending on air damping and fabrication errors. Under the present conditions, the sensitivities of the sensor in the X- and Y-axes were 0.693 and 0.154 pF/g, respectively. The cross-axis sensitivities in the X- and Y-axis directions were only 0.014 and 0.08%, respectively. The findings of this study are useful for the computation and development of two-axis acceleration sensors with insignificant cross-axis sensitivities.

References

1 L. Y. Sian and W. K. Ann: Micromachines **10** (2019) 50. https://doi.org/10.3390/mi10010050
2 W. Ying, Z. Xiaofeng, and W. Dianzhong: Sensors **20** (2020) 1780. https://doi.org/10.3390/s20061780
3 R. Kang, W. Xiaoli, Z. Shaolin, Z. Mengqi, H. Chenyuan, L. Huafeng, and T. Liang-Cheng: Micromachines **10** (2019) 380. https://doi.org/10.3390/mi10060380
4 Y. Wang, J. Zhang, Z. Yao, C. Lin, T. Zhou, Y. Su, and J. Zhao: IEEE Sens. J. **18** (2018) 7023. https://doi.org/10.1109/JSEN.2018.2852647
5 Y. Yin, Z. Fang, Y. Liu, and F. Han: Sensors **19** (2019) 1544. https://doi.org/10.3390/s19071544
6 D. Hussamud, I. Faisal, and L. Byeungleul: Micromachines **12** (2021) 902. https://doi.org/10.3390/mi12080902
7 A. R. Sankar and S. Das: Sens. Actuators, A **189** (2013) 125. https://doi.org/10.1016/j.sna.2012.09.025
8 Y. C. Yuan, H. Charm, C. Ting, C. Quang, and W. An: Microelectron. Eng. **279** (2023) 112044. https://doi.org/10.1016/j.mee.2023.112044
9 H. Qifang, Z. Yangxi, G. Chengchen, and H. Yilong: Micro Nano Lett. **69** (2011) 510. https://doi.org/10.1049/mnl.2011.0137
10 Z. Minghui, W. Xueyong, V. Hongwu, and W. Hairong: Smart Mater. Struct. **29** (2020) 085029. https://doi.org/10.1088/1361-665X/ab99d8
11 H. Jianqiang, Z. Zhengqian, N. Wenju, H. Rongyu, and D. Lizhen: Sens. Actuators, A **283** (2018) 17. https://doi.org/10.1016/j.sna.2018.09.040
12 A. Sthuthi, G. Nithya, K. N. Kumar, and S. S. Ramya: Materials Today Proc. (2023). https://doi.org/10.1016/j.matpr.2023.05.569
13 Y. Xiao, F. Hu, Y. Zhang, J. Zheng, and S. Qin: Sensors **22** (2022) 641. https://doi.org/10.3390/s22020641
14 K. Kim, Y. Sun, R. M. Voyles, and B. J. Nelson: IEEE Sensors J. **7** (2007) 344351. https://doi.org/10.1109/ROBOT.2006.1641723
15 P. Baranov, T. Nesterenko, E. Barbin, A. Koleda, S. Tanaka, T. Tsukamoto, I. Kulinich, D. Zykov, and A. Shelupanov: Sens. Rev. **39** (2019) 670. https://doi.org/10.1108/SR-05-2018-0133
16 R. Legtenberg, A. W. Groeneveld, and M. Elwenspoek: J. Micromech. Microeng. 6 (1996) 320. https://doi.org/10.1088/0960-1317/6/3/004
17 B. Wedyan, B. Sumana, M. Hussain, and M. Hussain: ACS Appl. Electron. Mater. **3** (2021) 504. https://doi.org/10.1021/acsaelm.0c00746

18 P. Francesca, M. Saleem, and S. Aurelio: Appl. Sci. **11** (2021) 1129. https://doi.org/10.3390/app11031129
19 K. S. Kumar, P. Chatterjee, B. Mukherjee, K. B. M. Swamy, and S. Sen: IEEE Trans. Instrum. Meas. **67** (2018) 196. https://doi.org/10.1109/TIM.2017.2761238
20 T. Q. Thong, N. Q. Long, D. Dzung, C. M. Hoang, and V. N. Hung: Microsyst. Technol. **20** (2014) 281. https://doi.org/10.1007/s00542-013-1947-0
21 N. N. Minh, H. S. Nhat, N. Q. Long, C. M. Hoang, and V. N. Hung: Micromachines **8** (2017) 42. https://doi.org/10.3390/mi8020042
22 Z. Wu, C. Yu, P. Bei, Y. Hui, Y. Huijun, L. Heng, H. Xiaoping: Adv. Mech. Eng. **373172** (2014) 1. http://dx.doi.org/10.1155/2014/373172
23 Q. Peng and Q. Hongwei: Sensors **13** (2013) 5720. https://doi.org/10.3390/s130505720
24 K. S. Rao, P. S. Mounika, P. Pavan, V. Guru, N. Dinesh, P. A. Kumar, K. Vineetha, K. G. Sravani: Microsyst. Technol. **25** (2019) 4197. https://doi.org/10.1007/s00542-019-04389-0
25 J. Ammar, S. Bijan, and G. Mohammadali: Mech. Mach. Theory **162** (2021) 104334. https://doi.org/10.1016/j.mechmachtheory.2021.104334
26 S. V. Iyer and T. Mukherjee: Technical Proc. 5th Int. Conf. Modeling and Simulation of Microsystems 1 (MSM, 2002) 186–189.
27 Q. Shi, S. Wang, A. Qiu, Y. Xu, and X. Ji: Proc. 1st IEEE Int. Conf. Nano Micro Engineered and Molecular Systems (2006) 242–245. https://doi.org/10.1109/NEMS.2006.334695
28 Y. Kang and L. Peng: Shock Vib. (2019) 8376781. https://doi.org/10.1155/2019/8376781
29 M. Bao: Analysis and Design Principles of MEMS Devices (Elsevier, 2005) 1–312.
30 M. Benmessaoud and M. Nasreddine: Microsyst. Technol. **19** (2013) 713. https://doi.org/10.1007/s00542-013-1741-z
31 Z. H. Zhang, W. Xueyong, D. Yanyu, J. Z. Jiang: Sens. Actuators, A **296** (2019) 79. https://doi.org/10.1016/j.sna.2019.06.051
32 W. Zhongye, F. Ronghui, S. Chengliang, W. Peng, and W. Guoqiang: Microelectron. Eng. **269** (2023) 111918. https://doi.org/10.1016/j.mee.2022.111918
33 G. Joan, M. Daisuke, O. Kazuo, M. Shkel, and S. Tomonori: J. Microelectromech. Syst. **28** (2018) 25. https://doi.org/10.1109/JMEMS.2018.2881209
34 J. Basu and T. K. Bhattacharyya: Microsyst. Technol. **17** (2011) 1557. https://doi.org/10.1007/s00542-011-1332-9
35 E. E. Moreira, B. Kuhlmann, F. S. Alves, and R. Dias: Sens. Actuators, A **307** (2020) 112005. https://doi.org/10.1016/j.sna.2020.112005
36 Z. Ahmed, C. Duruaku, F. Edalatfar, M. Moallem, and B. Bahreyni: Micromachines **14** (2023) 1188. https://doi.org/10.3390/mi14061188
37 M. Zakriya, A. Gill, and R. Mahmoud: IEEE Sens. Lett. **2** (2017). https://doi.org/10.1109/LSENS.2017.2756108
38 F. Hamed, K. Mills, and L. Cleghorn: Microsyst. Technol. **15** (2009) 1815. https://doi.org/10.1007/s00542-009-0895-1

About the Authors

Nguyen Van Cuong received his B.S. and M.S degrees from Le Quy Don University, Vietnam, in 2013 and 2016, respectively. Since 2016, he has been a lecturer at Le Quy Don University, Vietnam. His research interests are in MEMS, bioengineering, and sensors.
(vancuong_hvkt@lqdtu.edu.vn)

Nguyen Van Duong received his M.Sc. degree in control engineering and automation from Le Quy Don University in 2017. Since December 2023, he has been a doctorate student of materials science at the International Training Institute for Materials Science, Hanoi University of Science and Technology, Hanoi, Vietnam. He is also a lecturer at FPT University. His research interests are in MEMS actuators and sensors. (duongnv44@fpt.edu.vn)

Bui Van Cuong received his B.S. and M.S. degrees from Le Quy Don University, Vietnam, in 2004 and and 2007, respectively, and his Ph.D. degree from Irkutsk National Research Technical University, Russia, in 2017. Since 2017, he has been a researcher at Le Quy Don University, Vietnam. His research interests are in MEMS, sensors, and artificial intelligence in mechanical engineering, and the optimal design of machines. (manhcuongkck@gmail.com)

Chu Manh Hoang received his M.Sc. degree from Hanoi University of Science and Technology (HUST), Hanoi, Vietnam, in 2007 and Dr. Eng. degree from Tohoku University, Japan, in 2011. In May 2018, Dr. Chu became an associate professor of physics, at HUST. He was promoted to full professor of physics in 2022. He is the author of more than 130 papers in journals and conference proceedings, has been granted 10 patents, and has written one book chapter and two books on plasmonics, MEMS sensors, and actuators. His interests are in developing research in micro/nano optics and microsystems. (hoang.chumanh@hust.edu.vn).